International Journal of Hydrogen Energy xxx (xxxx) xxx

Contents lists available at ScienceDirect

International Journal of Hydrogen Energy

journal homepage: www.elsevier.com/locate/he

Hydrogen storage on the lithium and sodium-decorated inorganic graphenylene

Nicolas F. Martins [a], Ary S. Maia [b], José A.S. Laranjeira [a], Guilherme S.L. Fabris [c], Anderson R. Albuquerque [d], Julio R. Sambrano [a,*]

[a] Modeling and Molecular Simulation Group, São Paulo State University, Bauru, SP, Brazil
[b] Chemistry Department, Federal University of Paraíba, 58051-900, João Pessoa, PB, Brazil
[c] Post-Graduate Program in Materials Science and Engineering, Federal University of Pelotas, 96010-610, Pelotas, RS, Brazil
[d] Chemistry Institute, Federal University of Rio Grande do Norte, 59078-970, Natal, RN, Brazil

ARTICLE INFO

Handling Editor: Dr M Mahdi Najafpour

Keywords:
Hydrogen storage
Biphenylene sheet
Graphenylene
Metal decoration
2D materials
DFT

ABSTRACT

Efficient H_2 storage is one of the keys to the energy transition toward global sustainability. Hydrogen energy sources on functionalized 2D materials by metals have been shown as promising alternatives for clean energy systems. In a particular way, we have demonstrated here that the inorganic graphenylene-like silicon carbide (IGP-SiC) weakly adsorbs H_2. At the same time, the Li/Na decoration significantly enhances the H_2 interaction, accommodating up to $48H_2$ molecules by a stronger physisorption. Also, scanning bond critical points (BCPs) confirms a great interaction between the Li(Na)@IGP-SiC systems and the hydrogen, a distinct scenario for the pristine IGP-SiC. Gravimetrically, hydrogen densities reach 8.27 wt% (Li) and 6.78 wt% (Na), exceeding the U.S. Department of Energy (5.6 wt%) benchmark. Regarding thermodynamic stability, the desorption temperatures at ambient conditions are suitable for hydrogen storage devices. Therefore, Li(Na)@IGP-SiC systems emerge as high-capacity hydrogen storage materials.

1. Introduction

Hydrogen has awakened the scientific community's interest as a smart choice to substitute non-sustainable sources due to their benefits, such as high efficiency and low environmental impact [1–4]. The procedures for hydrogen generation are well-known, such as water electrolysis [5], photochemical [6], photoelectrochemical [7], and photobiological [8]; however, hydrogen storage for mobile transport is still a significant issue. In this sense, H_2 storage mechanisms such as compressed [9,10] and cryogenic hydrogen [11,12], or both simultaneous strategies (cryo-compression) [13], are today the most used. Also, physical adsorption in solids has been reported as a promising alternative, enhancing the storage rate under adsorption and desorption processes [14,15].

The hydrogen physisorption can be indicated as a potential H_2 storage device due to the no presence of chemical bonds or a high degree of interaction between the adsorptive and the substrate (solid) and the reversible operation in moderate pressures (30 bar) and lower temperatures [16]. However, at room temperature and high pressure, such as 90 bar, the interaction between hydrogen and the substrate becomes weaker by the appearance of van der Waals forces, mitigated by operating in cryogenic temperatures [17].

As is known, several materials have shown good performance for hydrogen storage; among these, the research of Dillon and co-workers [18] investigates the single-walled carbon nanotubes (SWCNTs) as a hydrogen storage system, with a rate of 5–10 wt% of hydrogen at ambient temperature. On the other hand, by applying a cryogenic treatment (77 K) and atmospheric conditions (1 bar), Castaldo and co-workers [19] added multi-walled CNTs into a polymeric matrix to form a robust nanocomposite with a great micropore volume, leading an H_2 storage capacity of 1.4 wt%.

From both theoretical and experimental points of view, ternary compounds based on LaN_5 were inspected by Lodziana and colleagues [20], which appoints several of them as favorable to stabilize the H_2 sorption/desorption due to the suitable hydride formation enthalpy. On the other hand, Mbonu and co-workers [21] indicate that the gravimetric densities of $KXCl_3$ (X = Be, Mg and Ca) halide perovskites are very sensitive to the cationic sizes of the group IIA elements, but not for

* Corresponding author.
E-mail address: jr.sambrano@unesp.br (J.R. Sambrano).

https://doi.org/10.1016/j.ijhydene.2023.10.328
Received 12 September 2023; Received in revised form 25 October 2023; Accepted 30 October 2023

the cell volume of the structures, and values of 5.866 wt% (Be), 4.516 wt % (Mg) and 3.649 wt% (Ca) are found. In addition, several nanostructures are widely reported in the literature for potential hydrogen storage systems, such as amide-halide systems [22,23], MOFs [24–26] and zeolites [27,28].

As mentioned previously by Zhou and co-workers [29] in the early 2010s, solid-state hydrogen storage devices guided by physical adsorption can be improved with systems disposing of large surface areas. Two-dimensional (2D) materials successfully meet this requirement due to their lower mass density and high surface-to-volume ratio [30,31]. In this sense, Li and co-workers [32] showed by density functional theory (DFT) simulations that the layered Ti_2N can store H_2 around ~8.6 wt%. Beyond this, it is reported by experimental and theoretical procedures that graphene and graphene-like nanosheets (h-BN, borophene, phosphorene, silicene) can be recognized as 2D hydrogen storage materials [33–37].

Taking into account, graphenylene (GP), also named 4-6-12 biphenylene, is a carbon monolayer with a periodic arrangement highlighted by its dodecagonal, hexagonal, and square rings [38,39], that can store hydrogen, as demonstrated firstly by Yadav and co-workers [40]. By a theoretical framework, the authors compared H_2 storage profiles of many 2D carbon allotropes, including GP and other porous carbon monolayers such as PHE-graphene, graphdiyne, and FSL-graphene, unveiled a hydrogen gravimetric density of about 2.6 wt% for GP when decorated by lithium atoms. Furthermore, Hussain and colleagues [35] reached an excellent gravimetric density of 6.14 wt% by employing alkaline earth metals to decorate the GP. Recently, a DFT-D3 study by Boezar and co-workers [41] elucidates the effect of transition-metal (TM) doping on hydrogen storage capacity, verifying that TM-doped GP could store $20H_2$ molecules. Therefore, it is noted that the graphenylene monolayer combined with a selective metal functionalization can be an exciting strategy to improve the hydrogen storage capacity, demanding new efforts to comprehend it, aiming at new perspectives on applying porous 2D materials in hydrogen technologies.

Considering the results mentioned above, the GP special arrangement also brings attention as a template for inorganic analogs (IGP), which can hold interesting properties [42–45]. The silicon carbide-based (IGP-SiC) was recently predicted using computational quantum-mechanical calculations [46]. The study reveals the thermal stability of IGP-SiC under 1200 K, good phonon dispersion, and optimal alkaline diffusion (Li, Na and K) on the 12-membered ring, which could be attractive for energetic applications. In 2022, Martins and co-workers [47] investigated the potential use of IGP-SiC as an anodic device for Na batteries. Besides the suitable open-circuit voltage (OCV) profile, IGP-SiC has a specific capacity of 610.46 $mAh.g^{-1}$, and the Na atoms are physisorbed on the nanosheet, which is the main factor for electrode charge and discharge process, and a good indicative for H_2 storage.

Therefore, by following the multifunctional nature of the recently predicted inorganic graphenylene based on SiC, this paper aims to study the IGP-SiC performance for hydrogen storage by lithium and sodium decoration (Li(Na)@IGP-SiC) by means of DFT computational simulations. The results were analyzed regarding the adsorption energies, gravimetric density, density of states and desorption temperature.

2. Computational method

All simulations were carried out using the periodic DFT approach implemented in the CRYSTAL17 package [48]. The B1WC hybrid functional [49] was adopted in conjunction with the triple-zeta valence with polarization (TZVP) [50] and the 6-311d11G [51] all-electron basis set to represent the Si and C centers, respectively, as performed in the previous works [46,52] to describe the IGP-SiC structure. The TZVP basis set was also applied for the Li, Na and H centers. To compare the level of theory followed by past studies [46,47] and applied here, the D3 correction developed by Grimme [53] was also used to consider the effect of the long-range London dispersion interactions. There is no D3 implementation in the B1WC functional, so the hybrid functional HSE06-D3 was used to guide more accurate comparisons using Grimme's correction for the Li(Na)@IGP-SiC nanosheets.

The Broyden–Fletcher–Goldfarb–Shanno (BFGS) [54] algorithm for Hessian updating, taking 0.0001 a.u. for convergence criteria on the gradient and 0.0004 a.u. for nuclear displacements, was adopted. All stationary points were characterized as a minimum by diagonalizing the Hessian matrix in terms of atomic coordinates and unit cell parameters. The threshold parameters for calculating the Coulomb and exchange bi-electronic integrals have been set to 8, 8, 8, 8 and 16 by invoking the TOLINTEG keyword in the CRYSTAL code to represent the overlap and penetration for Coulomb integrals, the overlap for Hartree-Fock (HF) exchange integrals and the first and second exchange pseudo-overlap, respectively. The Pack-Monkhost [55] and Gilat [56] net are described by a 6 x 6 x 1 *k*-point mesh, corresponding to 20 independent k-points in the irreducible part of the Brillouin zone integration.

The band structure, the density of states (DOS) and atomic charge analysis were calculated using the same *k*-point sampling method to diagonalize the Fock matrix during the optimization. The Bader analysis was conducted [57] to understand the interaction between hydrogen molecules with pristine IGP-SiC and Li(Na)@IGP-SiC systems. On the other hand, it is analyzed the electron density topology via the Quantum Theory of Atoms in Molecules (QTAIM) proposed by Bader and Essen [58] and posteriorly extended for crystals by Gatti [59]. The 3D visualization and post-processing of data from the topological analyses were performed in the TopIso3D viewer [60], a graphical user interface program for Topond [61] calculations.

The H_2 adsorption on the IGP-SiC pristine and Li(Na)@IGP-SiC systems were evaluated by calculating the adsorption energy (E_{ads}), which is defined by the following equation:

$$E_{ads} = \frac{E_{Li(Na)@IGP+H_2} - E_{Li(Na)@IGP} - nE_{H_2} + E_{BSSE}}{n} \quad (1)$$

where $E_{Li(Na)@IGP+H_2}$ is the total energy/unit cell of the Li(Na)@IGP-SiC systems plus H_2 molecules, $E_{Li(Na)@IGP}$ is the total energy/unit cell of the Li(Na)@IGP-SiC systems, E_{H_2} is the total energy of the isolated H_2 molecule, and n is the number of H_2 molecules. The E_{BSSE} refers to the energy correction due to the basis set superposition error (BSSE), which is considered *a posteriori* counterpoise method (CP) [62].

Another essential measurement, the hydrogen gravimetric density in weight (wt%), is calculated by the equation:

$$C_g = \frac{nW_{H_2}}{nW_{H_2} + W_{Li(Na)@IGP}} \quad (2)$$

From the calculated adsorption energy, the desorption temperature (T_D can estimate the thermal stability of hydrogen charge/release cycles. Here, the T_D is calculated using the van't Hoff equation [63,64], at atmospheric pressure (P = 1 bar):

$$T_D = |E_{ads}| \frac{R}{\Delta S\, K_B} \quad (3)$$

where K_B, ΔS and R are the Boltzmann constant, the entropy of the dehydrogenation reaction (130 $J\ K^{-1}\ mol^{-1}$) [65] and the universal ideal gas constant, respectively.

3. Results and discussion

3.1. Adsorption model

The IGP-SiC structure belongs to the space group *P6/m* (no. 186), with lattice parameters $a = b = 8.35$ Å. In a (2*x*2) supercell, the IGP-SiC is composed of different rings (dodecagonal, hexagonal and square), and three Si–C bonds are unveiled at a measure of 1.73 Å (Si_1–C_1), 1.78 Å (Si_1–C_2) and 1.83 Å (Si_1–C_3). This special IGP-SiC architecture leads to eight adsorption sites, as demonstrated in Fig. 1. Therefore, the metal

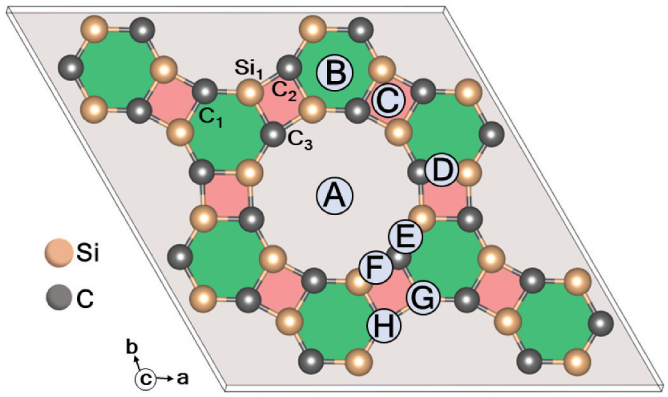

Fig. 1. IGP-SiC (2*x*2) supercell with the adsorption sites available to start the storage of metals (Li and Na) and H_2.

and H_2 adsorption can be performed by examining the center of dodecagonal (A), hexagonal (B) and square (C) rings, the bridge sites (D, E and F), as well as above the silicon (G) and carbon (H) atoms. Also, all adsorptions on the IGP-SiC nanosheet were made to allow symmetry conditions, i.e., inserting the atoms below and above the surface.

3.2. Hydrogen storage on pristine IGP-SiC

Considering the possible adsorption sites (see Fig. 1), the most appropriate place to initiate the H_2 saturation was investigated in terms of the adsorption energy. The E_{ads} values are 60 meV for A, B and C rings, while the bridge sites (D, E and F) have 0.05 eV, the same for the H site, above the carbon atom. Finally, it is found that the G site is the most stable place to adsorb the H_2 molecules (E_{ads} = 20 meV), whose adsorption is registered in Fig. 2.

Table 1 shows a detailed "fingerprint" of the adsorption results from the addition of $4H_2$ (2 molecules above and below) to $24H_2$ (12 above

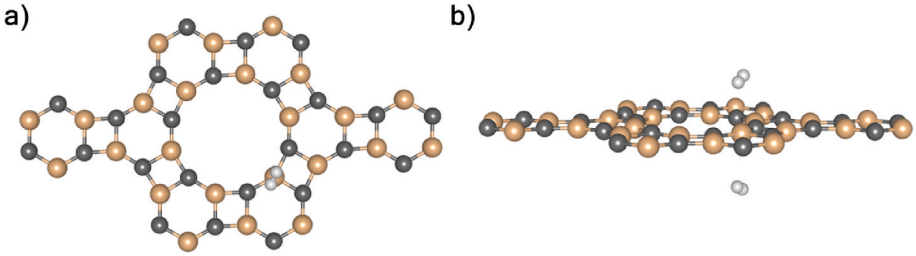

Fig. 2. **(a)** Top and **(b)** perspectives view of the single H_2 adsorption on the most stable site (G) of IGP-SiC (2*x*2) supercell.

Table 1
Average H–H (d_{H-H}) and H-IGP (d_{H-IGP}) bond lengths, in Å, adsorption energies (E_{ads}), in eV, and the average Bader charges (Q^H_{ave}), in e^-, for the H_2 adsorption on the pristine IGP-SiC.

System	d_{H-H} (Å)	d_{H-IGP}	E_{ads}	Q^H_{ave}
IGP + $4H_2$	0.75	2.99	0.022	−0.004
IGP + $6H_2$	0.75	2.89	0.012	−0.004
IGP + $12H_2$	0.75	2.85	−0.001	−0.004
IGP + $18H_2$	0.75	2.86	−0.004	−0.004
IGP + $24H_2$	0.75	2.84	−0.007	−0.005

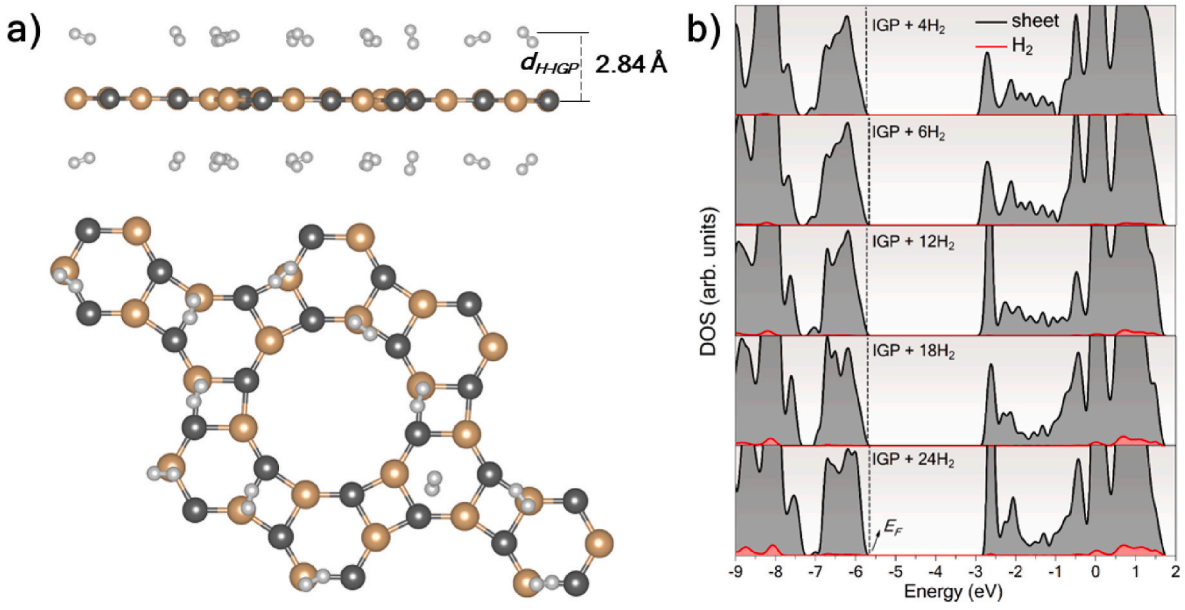

Fig. 3. **(a)** Side and top view of $24H_2$ molecules above and below the pristine IGP-SiC and **(b)** density of states (DOS) for $4H_2$, $6H_2$, $12H_2$, $18H_2$ and $24H_2$ adsorbed molecules. The arbitrary scale for DOS intensity is expressed in 0–1500.

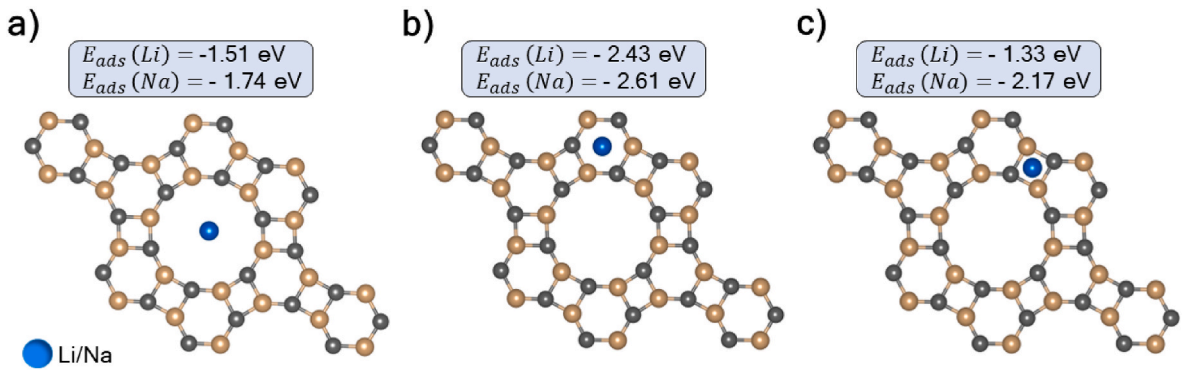

Fig. 4. Single Li and Na adsorption on the **(a)** dodecagonal, **(b)** hexagonal and **(c)** square sites of IGP-SiC nanosheet, and the adsorption energies (E_{ads}) for each ring. The E_{ads} for single Li(Na) adsorption on D, E, F, G and H sites are −2.38 eV (−2.50 eV).

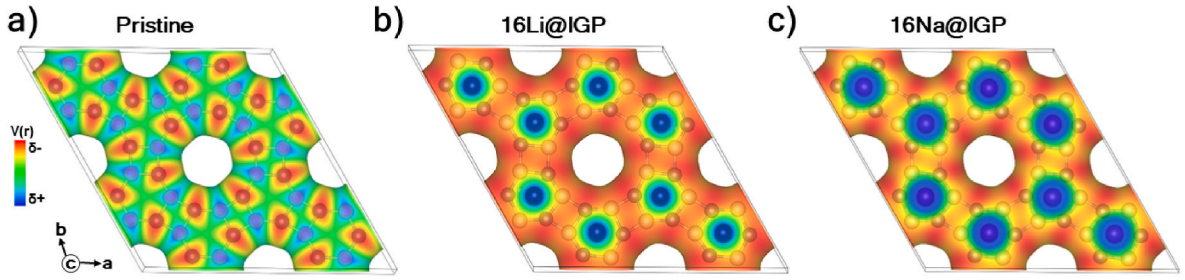

Fig. 5. Top view of the electrostatic potential maps [V(r)] (0.05 a.u. isodensity) for **(a)** pristine IGP-SiC and the IGP-SiC with 16 **(b)** Li and **(c)** Na atoms.

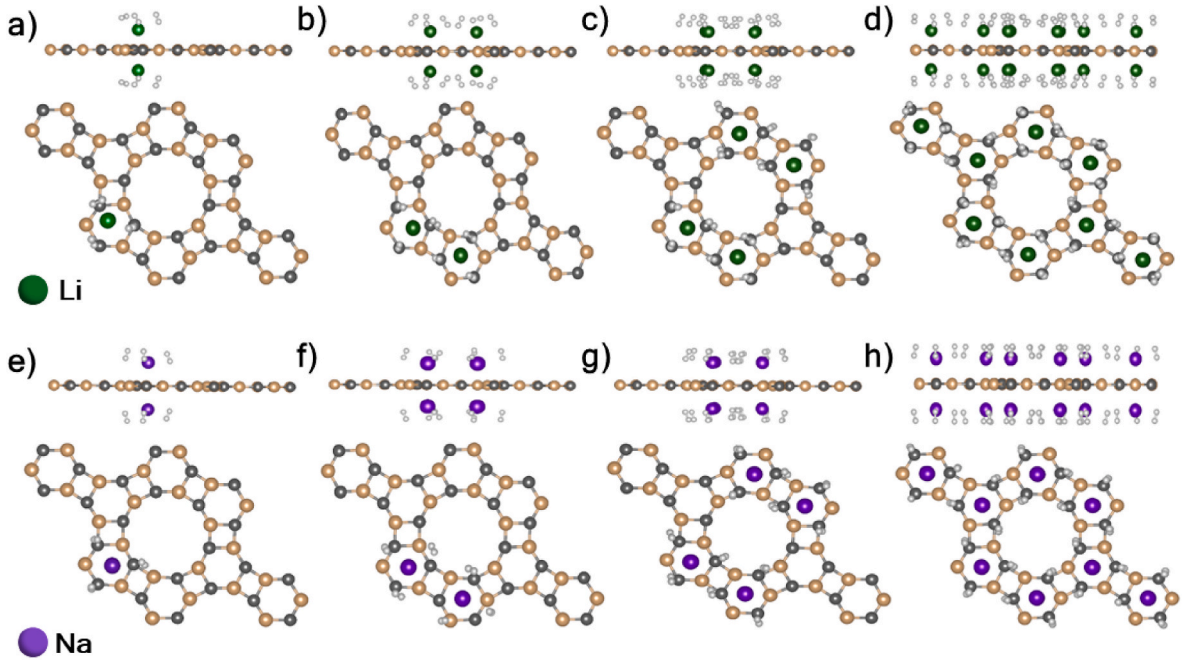

Fig. 6. H_2 adsorption in nLi(Na)@IGP-SiC + xH_2 structures, where n and x are **(a, e)** 2 and 6, **(b, f)** 4 and 12, **(c, g)** 8 and 24 and **(d, h)** 16 and 48, respectively.

and below) on the IGP-SiC pristine nanosheet. The adsorption energies for all systems can be classified as van der Waals interactions. The E_{ads} become negative by the adsorption of more H_2 molecules since the distance between H_2 and IGP-SiC is decreased, changing from 2.99 Å to 2.84 Å for the maximum adsorption configuration. Also, the Bader analysis shows a small charge transference from H_2 to the IGP-SiC nanosheet, in agreement with the weak interaction demonstrated by the E_{ads} values.

The final configuration for H_2 adsorption on the pristine IGP-SiC can be seen in Fig. 3a. From the top view, it is confirmed that H_2 molecules move toward the Si atom. The IGP-SiC planar structure maintains its architecture with the weak H_2 physisorption, and the leak of interaction is also verified by the DOS plot (see Fig. 3b). The band gap energy (E_{gap}) of IGP-SiC (3.22 eV) does not change, demonstrating that H_2 molecules do not affect the electronic structure of pristine IGP-SiC. Therefore, it is concluded that H_2 adsorption on the pristine IGP-SiC is

Table 2
H–H bond length (d_{H-H}) and the minimum and maximum distances between the H atom and the Li(Na) metal ($d^{H-Li(Na)}_{min/max}$), in Å, gravimetric densities (C_g), in wt%, and the average H_2 adsorption energies (E_{ads}), in eV. The values in parentheses for E_{ads} refers to the Li(Na)@IGP-SiC nanosheets without hydrogen molecule.

System	d_{H-H}	$d^{H-Li(Na)}_{min}$	$d^{H-Li(Na)}_{max}$	C_g	E_{ads}
Li					
2Li@IGP+6H_2	0.76	2.01	2.28	1.22	−0.147 (−1.58)
4Li@IGP+12H_2	0.76	2.02	2.25	2.39	−0.153 (−1.67)
8Li@IGP+24H_2	0.76	2.02	2.25	4.54	−0.154 (−1.70)
12Li@IGP+36H_2	0.77	2.03	2.27	6.49	−0.158 (−1.73)
16Li@IGP+48H_2	0.77	2.05	2.23	8.27	−0.140 (−1.69)
Na					
2Na@IGP+6H_2	0.76	2.36	2.54	1.19	−0.109 (−1.07)
4Na@IGP+12H_2	0.76	2.41	2.54	2.24	−0.125 (−1.26)
8Na@IGP+24H_2	0.76	2.41	2.54	4.05	−0.126 (−1.22)
12Na@IGP+36H_2	0.76	2.43	2.52	5.54	−0.121 (−1.20)
16Na@IGP+48H_2	0.76	2.46	2.47	6.78	−0.099 (−1.15)

thermodynamically unfavorable, demanding new strategies to improve hydrogen storage, such as the metal-decoration presented in the follower topic.

3.3. Hydrogen storage on the Li and Na-decorated IGP-SiC

The Li and Na decoration on the IGP-SiC was first analyzed by single Li and Na adsorption on the possible sites of IGP-SiC, as depicted in Fig. 1. Following the reported result of our previous work concerning the Na adsorption on the IGP-SiC structure [47], the metals adsorb preferably on the hexagonal ring (site B) with $E_{ads} = -2.43$ eV and $E_{ads} = -2.61$ eV for Li and Na, respectively. It is thermodynamically more stable than the dodecagonal (A) and square (B) rings and also than the D, E, F, G and H sites, whose values are −2.38 eV (−2.50 eV) for Li(Na) atoms. Fig. 4 shows the Li and Na single adsorption on the IGP-SiC for the main rings.

Therefore, the metals filled all hexagonal sites, leading to 8 Li(Na) atoms above and below the IGP-SiC nanosheet in the final step. This work uses a proportion of one metal (Li and Na) for three hydrogen molecules due to the composition of the hexagonal rings (three atoms of Si and C). First, it is important to note that one of the reasons for functionalizing the IGP-SiC with Li and Na atoms is the modification of the electron density around the monolayer, as evidenced by the electrostatic potential maps obtained in Fig. 5. The presence of Li and Na metals changes the charge electron density from a significant Li(Na)–Li (Na) repulsion that could be essential to insert H_2.

Fig. 6 shows the steps for H_2 adsorption, highlighting the 2, 4, 8 and 16 metal-decorated IGP-SiC with adsorbed 6H_2, 12H_2, 24H_2 and 48H_2 molecules. As mentioned above, the Li and Na-decorated IGP-SiC can adsorb 48H_2 molecules, 24H_2 up and down the nanosheet. As demonstrated, the Li and Na adsorption changes the H_2 mobility, leading to a non-registered scenario compared to pristine IGP-SiC. The hydrogen molecules are closest to the C atoms (top view), contrary to the result presented for undecorated IGP-SiC. However, because of the Na–Na repulsion and their high atomic radius, the H_2 molecules on Na-decorated IGP-SiC are shifted to the dodecagonal border of the nanosheet, differently from Li@IGP-SiC systems. Therefore, the metal decoration significantly changes the H_2 distribution on the IGP-SiC nanosheet, rearranging the hydrogen movement towards the Li and Na-decorated IGP-SiC.

The behavior of Li and Na atoms above and below the IGP-SiC also differ since the Li–Li distance across the hexagonal center is 0.81 Å lower than visualized by Na–Na in the final configuration with 48H_2 adsorbed molecules. Inspecting the Li@IGP-SiC with 48H_2 molecules, the minimum and maximum H–Li measures are 2.05 Å and 2.23 Å, respectively, while all H–Na bond lengths are almost equal (~2.47 Å). The H_2 disposition after fully optimizing Li and Na decoration was also noted. The Li adsorption induces a final H_2 configuration more inclined than the Na@IGP-SiC system, as seen by the side view in Fig. 6. These results could justify the small variation of H–H bond length from 0.75 to 0.77 Å for the 16Li@IGP-SiC system with 48H_2 molecules. The final configurations for 16Li(Na)@IGP-SiC plus 48H_2 molecules were also noted with the HSE06-D3 setup (see Fig. S1 of the Supplementary Information file), whose behavior is similar to the B1WC hybrid functional executed in this work.

Table 2 shows the structural results for all H_2 adsorption steps on the

Table 4
Topological descriptors of each BCP found for the pristine IGP-SiC and Li(Na)@IGP-SiC systems with H_2 molecules. H–H[1] represents a weak interaction between hydrogen molecules adsorbed on the surface of the system and H–H[2] the strong covalent character related to the bonds between the two hydrogen atoms in the H_2 molecules.

BCP	ρ_b	$\nabla^2\rho_b$	$\lvert V_b\rvert/G_b$	H_b/ρ_b	Bond type
IGP+24H₂					
H–H[1]	0.002	0.006	0.701	0.178	vdW
H–C	0.008	0.019	0.862	0.070	vdW
H–Si	0.008	0.019	0.884	0.059	vdW
Si–C	0.135	0.275	1.592	−0.731	Transitory
H–H[2]	0.250	−0.971	583.249	−0.971	Covalent
16Li@IGP-SiC+48H₂					
H–H[1]	0.005	0.016	0.747	0.154	vdW
H–C	0.014	0.037	0.887	0.066	vdW
H–Li	0.009	0.051	0.731	0.302	vdW
Li–C	0.014	0.071	0.845	0.164	vdW
Si–C	0.123	0.251	1.578	−0.690	Transitory
H–H[2]	0.242	−0.911	99.164	−0.952	Covalent
16Na@IGP-SiC+48H₂					
H–H[1]	0.005	0.016	0.759	0.150	vdW
H–C	0.014	0.034	0.885	0.061	vdW
H–Na	0.009	0.039	0.736	0.238	vdW
Na–C	0.013	0.049	0.856	0.119	vdW
Si–C	0.120	0.229	1.595	−0.689	Transitory
H–H[2]	0.238	−0.885	68.272	−0.943	Covalent

Table 3
Bader charges (e⁻) analysis of H_2 adsorption on the Li(Na)@IGP-SiC systems.

System	Q^{Si}_{ave}	Q^{C}_{ave}	$Q^{Li(Na)}_{ave}$	$Q^{Li(Na)}_{max}$	$Q^{Li(Na)}_{min}$	Q^{H}_{ave}	Q^{H}_{max}	Q^{H}_{min}
Li								
2Li@IGP+6H_2	+0.510	−0.514	+0.680	+0.680	+0.680	−0.005	+0.029	−0.034
4Li@IGP+12H_2	+0.450	−0.528	+0.692	+0.698	+0.686	−0.010	+0.041	−0.069
8Li@IGP+24H_2	+0.355	−0.544	+0.687	+0.693	+0.682	−0.008	+0.052	−0.085
12Li@IGP+36H_2	+0.269	−0.578	+0.681	+0.681	+0.681	−0.007	+0.060	−0.084
16Li@IGP+48H_2	+0.208	−0.619	+0.682	+0.685	+0.677	−0.008	+0.068	−0.082
Na								
2Na@IGP+6H_2	+0.470	−0.542	+0.809	+0.809	+0.809	−0.005	+0.034	−0.046
4Na@IGP+12H_2	+0.416	−0.543	+0.787	+0.787	+0.786	−0.016	+0.044	−0.104
8Na@IGP+24H_2	+0.356	−0.564	+0.777	+0.777	+0.776	−0.031	+0.051	−0.119
12Na@IGP+36H_2	+0.274	−0.616	+0.767	+0.767	+0.767	−0.026	+0.061	−0.110
16Na@IGP+48H_2	+0.229	−0.642	+0.763	+0.763	+0.762	−0.028	+0.060	−0.111

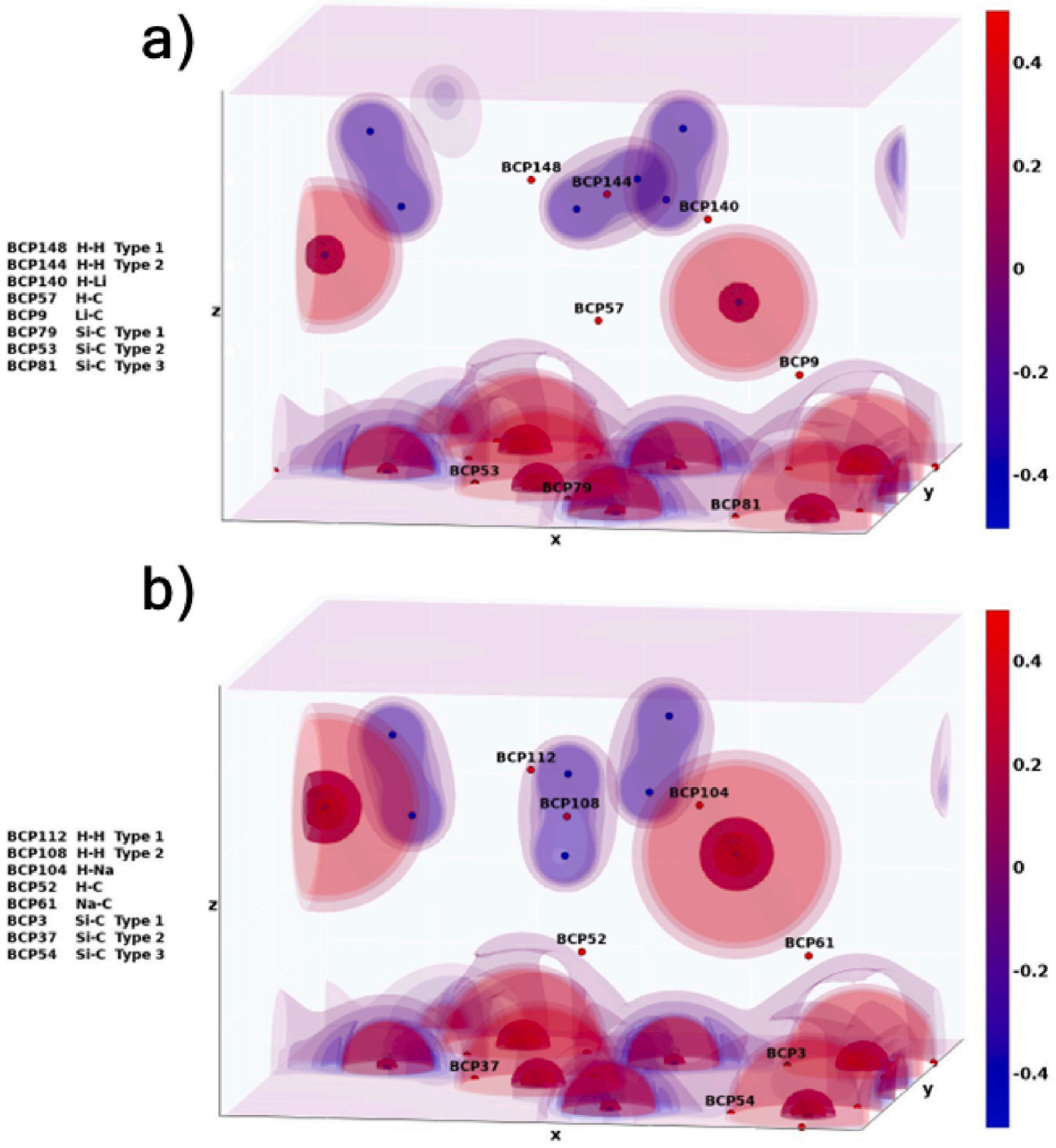

Fig. 7. 3D isosurfaces maps of the Laplacian of the electron density (SURFLAPP) generated by the TopIso3D viewer, highlighting the BCPs for **(a)** 16Li@IGP-SiC and **(b)**16Na@IGP-SiC with 48H_2 molecules.

metal-decorated IGP-SiC. Besides this, the adsorption energies were computed to comprehend the interaction of H_2 on the IGP-SiC under Li and Na decoration. At the same time, the adsorption energies of Li(Na)-decorated IGP-SiC without H_2 are also observed by the values in parenthesis. Based on this last analysis, it is clarified that E_{ads} values have a small decrease with the increase of metal decoration up and down the IGP-SiC, leading to a more stable nanosheet with the Li(Na) addition. Stronger adsorption was observed for all Li(Na)@IGP-SiC systems without H_2, which can be seen by the intensity of the electron density depicted in Fig. 5.

When the H_2 adsorption occurs, the adsorption energies of Li(Na) @IGP-SiC plus nH_2 molecules have a larger decrease in these values. Nevertheless, within a range of −0.140 eV and −0.158 eV, the H_2 adsorption on Li@IGP-SiC systems is characterized by a physisorption mechanism. It is detected a similar trend to the Na@IGP-SiC nanosheets, although lower E_{ads} values are registered (−0.099 eV to −0.126 eV). All physical adsorptions visualized for H_2 on the Li(Na)@IGP-SiC are stronger than the calculated in pristine configuration, indicating a great effect of the metal decoration on these systems. In addition, Table S1 shows the computed values of adsorption energy and distances of H_2 on the Li(Na)@IGP-SiC nanosheets from the HSE06-D3 framework. Again, the trend is very similar, and the nature of adsorption is the same.

In Table 2, the gravimetric density is also depicted. The Li@IGP-SiC and Na@IGP-SiC systems have gravimetric densities of about 8.27 wt% and 6.78 wt%, respectively. These values are superior to other structures investigated for hydrogen storage, such as tetragonal SiC [66], Ni MOF [67], graphene oxide [68], MoS_2 [69] and borophene [70], and lower than the found for graphyne-like structures [71,72]. Additionally, the IGP-SiC performs with a higher capacity than studies about graphenylene [40,41,73]. In terms of H_2 storage on biphenylene-like nanosheets, we found a superior gravimetric density than the Li and Na-decorated biphenylene reported by Kaewmaraya and co-workers

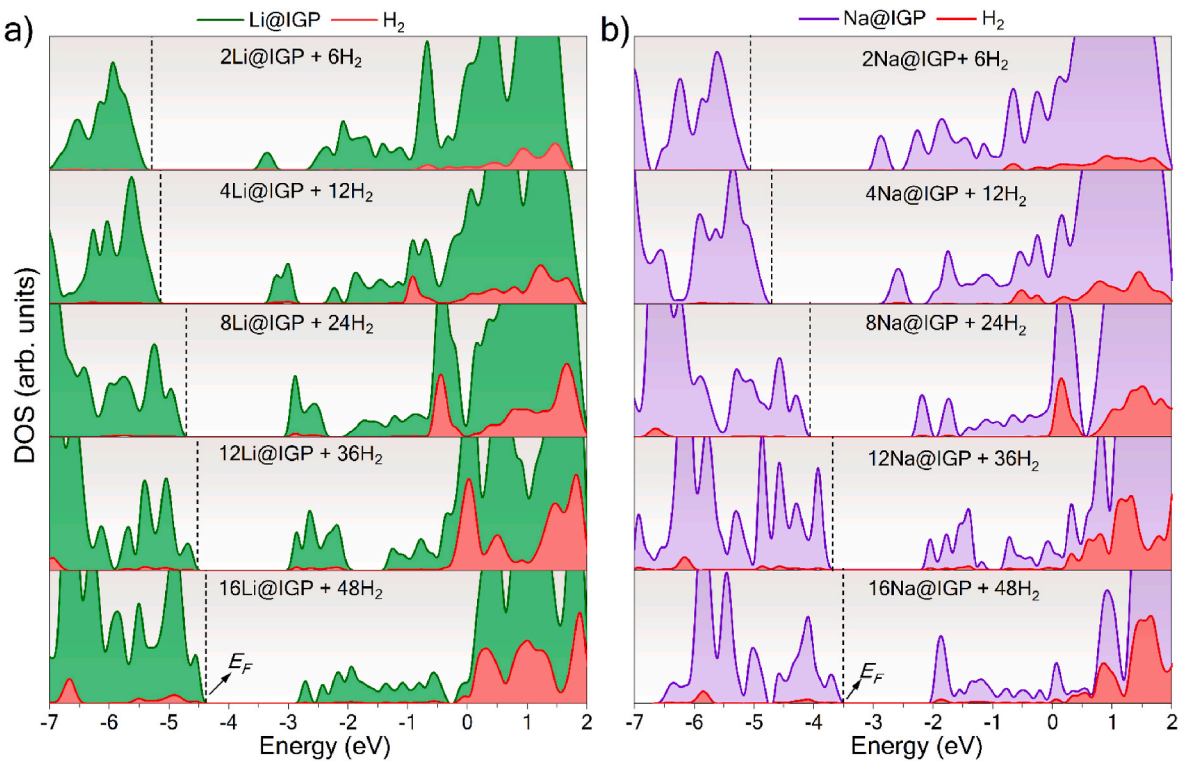

Fig. 8. Density of states (DOS) for H_2 adsorption on **(a)** Li and **(b)** Na@IGP-SiC systems. The arbitrary scale for DOS intensity is expressed in 0–1500.

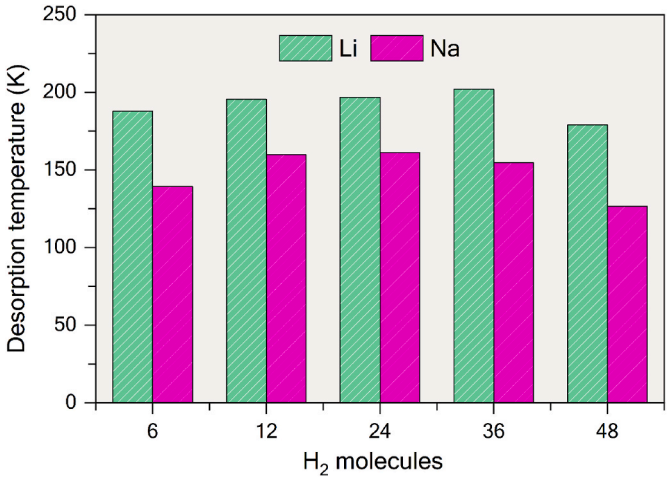

Fig. 9. Desorption temperatures for H_2 adsorption on the Li and Na-decorated IGP-SiC nanosheets.

[74], about 6.76 wt% (Li) and 6.66 wt% (Na), and especially for Li@IGP-SiC system, a greater hydrogen capacity than the 7.52 wt% found for the vanadium-decorated biphenylene [75]. At the same time, our values are lower than the Ca-decorated graphenylene studied by Pan and co-workers [76], 8.57 wt% by weight, which is caused by the metal and H_2 adsorption in the middle of the dodecagonal ring. However, as demonstrated in Fig. 4a, it is not the most favorable site for metal functionalization due to the leak of electronic density and reactivity in the region, leading to a weak interaction between hydrogen and solid. Beyond that, our results exceed the gravimetric storage capacity targeted by the U.S. Department of Energy (DOE), about 5.5 wt% [77,78].

Table 3 displays the Bader analysis of the Li and Na effect on the IGP-SiC nanosheet and the H_2 interaction through the charge transfer. In the pristine configuration, the Si and C atoms of IGP-SiC have $+0.513e^-$ and $-0.510e^-$, respectively. Since Si and C electronegativities are higher than Li and Na, the metal decoration greatly redistributes the charges around the IGP-SiC nanosheet. Under Li functionalization, the C atoms become more negative ($-0.510e^-$ to $-0.619e^-$). At the same time, the Li–Si is the main interaction where the electric charge from the metal is almost fully transferred to the Si atom. Therefore, the Li atoms are in a depleted region with $+0.682e^-$ in the 16Li@IGP-SiC configuration.

Concerning the H_2 molecules, as expected, Li atoms also transfer charge for this interaction, whose amount is superior to the registered for H atom on pristine IGP-SiC. Similar results are found for Na decoration. For Na@IGP-SiC systems, the charge transference from the metal to H atoms is more evidenced, varying from $-0.005e^-$ to $-0.031e^-$. Also, the Na atomic charge magnitude on H_2 adsorption is bigger than Li, also performing as a remarkable depletion region, in agreement with our previously reported study [47].

The pristine and functionalized IGP-SiC systems with 24 and 48H_2 molecules, respectively, were topologically analyzed based on the QTAIM Theory, identifying their main descriptors for their different bond critical points (BCPs), namely the BCP electron density (ρ_b), the Laplacian of the electron density ($\nabla^2\rho_b$), the adimensional ratio ($|V_b|/G_b$) and the bond degree (H_b/ρ_b). These results are summarized in Table 4, where the mean values of the descriptors with their respective standard deviations are presented. The representation of the BCPs through the mean values of their descriptors was possible since the calculated standard deviations were low.

The first fact worth mentioning is that all three systems presented two different types of H–H BCPs, one representing a weak interaction between hydrogen molecules adsorbed on the surface of the system (called $H–H^1$ or Type 1) and another with a strong covalent character related to the bonds between the two hydrogen atoms in the H_2 molecules (called $H–H^2$ or Type 2). According to the classifications of chemical interactions traditionally observed in the literature [79,80], the Si–C BCPs and $H–H^2$ bonds for all three systems present covalent character due to the negative values of the bond degree, although intermediate values between 1 and 2 for the $|V_b|/G_b$ ratio identifies the

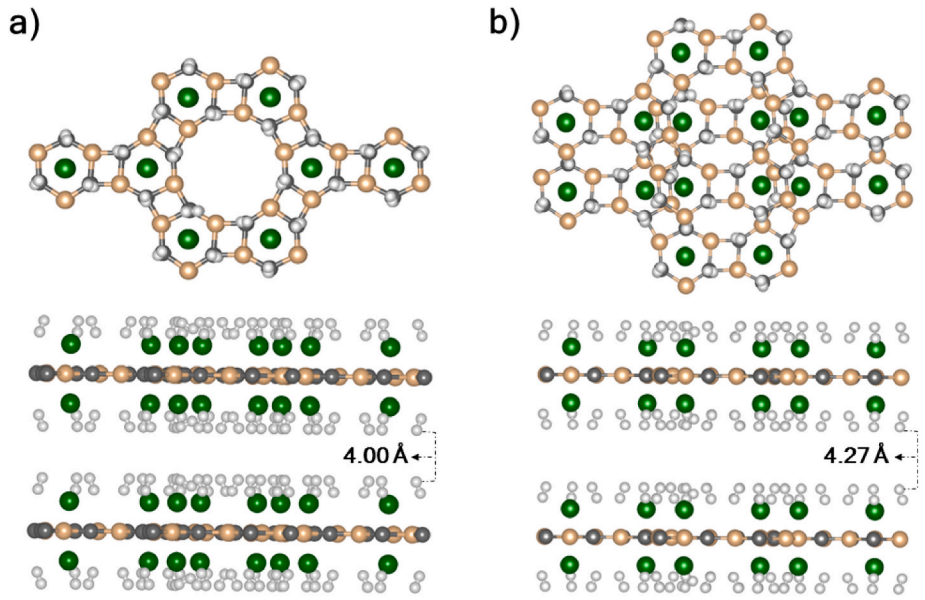

Fig. 10. Two possible stackings of Li(Na)@IGP-SiC systems by **(a)** symmetrical and **(b)** shifted arrangement.

Si–C BCPs as belonging to a transitory interaction between pure, shared and closed-shell interactions. This trend can be observed by the plot of 3D isosurfaces maps of Laplacian of electron density (SURFLAPP), shown in Fig. 7, which allows the visualization of all BCPs in 16Li(Na) @IGP-SiC systems with $48H_2$ molecule.

The high values of the $|V_b|/G_b$ ratio confirms the character of a pure shared shell interaction for the $H–H^2$ bonds, as visualized through BCP144 and BCP108 in Fig. 7a and b, respectively. However, the sharp drop in the value of this descriptor for the 16Li(Na)@IGP-SiC systems with $48H_2$ proves the influence of metals on hydrogen molecules in the adsorption process. All other BCPs descriptor values confirm them as weak Van der Waals-type interactions.

The electronic properties were also analyzed employing the DOS (see Fig. 8). It can be noted that the H_2 contribution on the IGP-SiC nanosheet increases with the number of H_2 molecules, a distinct behavior denoted for the pristine IGP-SiC. Furthermore, there are more H_2 orbitals located at the middle and the high levels of the conduction band (CB), while the Fermi level drastically changes from the increment of hydrogen molecules. Thence, the E_{gap} of pristine IGP-SiC is widely reduced from 3.22 eV to ~1.50 eV for Li and Na-decorated IGP-SiC. Nonetheless, the DOS figure illustrates that the interaction between H_2 and the metal closes the E_{gap} of IGP-SiC.

Considering the practical uses of hydrogen storage devices, very strong and weak interactions are undesirable. Since H_2 is strongly bonded with the substrate, chemisorption can be characterized, and desorption cannot happen. On the contrary, weak interaction between hydrogen and surface does not guarantee reversible uptake and unloading mechanisms. Hence, the desorption temperature (T_D) at ambient conditions is evaluated to comprehend the capability of Li and Na-decorated IGP-SiC nanosheets for a reversible use of H_2 molecules (see Fig. 9). As mentioned, the desorption temperatures increase with the magnitude of the adsorption energies. The H_2 on the Li(Na)@IGP-SiC structures presents a desorption temperature in the 179–202 K (126–161 K) ranges. These results indicate that average T_D values for Li and Na-decorated IGP-SiC are much bigger (~5.8 and ~4.5 times, respectively) than the critical point of hydrogen (33 K). For comparison purposes, a range of small desorption temperatures for H_2 on the pristine IGP-SiC (1–28 K) is found, confirming again that the undecorated IGP-SiC nanosheet is unsuitable for hydrogen storage.

In view of promoting a better comprehensive study of a large-scale IGP-SiC prototype as an H_2 storage platform, two stacking models were built considering the final metal-functionalized systems (see Fig. 10). Here, only the stacking originated by the 16Li@IGP-SiC system was considered due to the similarities with the Na functionalization. These analyses suggest 4.0 Å as the interlayer distance (H–H) between the functionalized layers, visualized by the symmetrical stacking of Fig. 10a. On the other hand, the second model is shifted on the xy-plane (0.25 Å in both directions) and characterized by a minimum H–H sloped bond length between the layers around 4.27 Å (see Fig. 10b). Using the TopIso3D viewer to create the SURFRHOO (electron density) maps (see Fig. S2), it is clarified that there is no interaction and charge transference between the layers on the configurations suggested here, as expected for the desired energetic application. The metal-metal interlayer distance is around 7 Å, a spacing considered appropriate for maintaining stronger physisorption of the system and the H_2 uptake, and closer to the theoretical/experimental reports for multilayer graphene [81] and mesoporous graphene oxide (GO) [82]. The multilayer scheme proposed here is expected to motivate further research by experimentalists to explore the interlayer spacing role in the decorated IGP-SiC sandwich and its promising use for large-scale energy storage applications.

4. Conclusions

This work predicts that IGP-SiC is a suitable 2D material for hydrogen storage systems when decorated by Li and Na atoms. The structural, electronic and topological properties were investigated for this purpose using DFT computational simulations. Firstly, the pristine IGP-SiC was considered. The results indicate an almost null interaction between H_2 molecules and the IGP-SiC nanosheet, endorsed by the adsorption energies, Bader analysis and the DOS plot. Taking into account, the functionalization of IGP-SiC by metals deserves considerable attention to improve the H_2 adsorption.

Firstly, it is unveiled that hexagonal is the most stable site to adsorb the Li and Na atoms. Thus, the IGP-SiC nanosheet can adsorb 16 metals around the structure, eight up and down the substrate, where each metal covers $3H_2$ molecules. In conclusion, the Li(Na)@IGP-SiC systems adsorb $48H_2$ molecules after final hydrogen adsorption. Adsorption energies of −0.158 eV (−0.099 eV) are obtained for the H_2 adsorption on 16Li(Na)@IGP-SiC nanosheets, which are stronger physisorption systems, different from the pristine IGP-SiC. The DOS plot confirms this trend, where the H orbitals contribute more with the increase of metal and H2 adsorption, signaling a great interaction between hydrogen and

Li(Na)@IGP-SiC structures. Also, the gravimetric densities were calculated with 8.27 wt% and 6.78 wt% capacities, which are superior to the suggested values by U.S. DOE (5.6 wt%). Finally, the registered desorption temperatures are higher than the critical point of hydrogen (33 K) in ambient conditions, recorded in 191 K and 148 K for Li and Na-decorated IGP-SiC nanosheets. Therefore, the aforementioned results set up the IGP-SiC as a promising 2D hydrogen storage system with high capacity and reversible H_2 storage.

Furthermore, in this initial study of the potential application of IGP-SiC as an H_2 storage device, two stacking models are suggested to be built and grown without the appearance of clusterization or chemisorption, which could assist experimentalists and other theoretical researchers to better comprehend the Li(Na)@IGP-SiC nanosheets with H_2 adsorbed for large-scale use.

Declaration of competing interest

The authors declare that they have no known competing financial interests or personal relationships that could have appeared to influence the work reported in this paper.

Acknowledgment

This work was supported by the Brazilian funding agencies FAPESP (13/07296–2, 20/01144-0, 22/00349–2, 22/03959–6, 22/14576–0), CNPq (grant no. 307213/2021–8, 150187/2023) and CAPES (grant no. 88887.827928/2023-00). The computational facilities were supported by resources supplied by the Modeling and Molecular Simulation group (São Paulo State University, Bauru, Brazil).

Appendix A. Supplementary data

Supplementary data to this article can be found online at https://doi.org/10.1016/j.ijhydene.2023.10.328.

References

[1] Contreras A. Hydrogen as aviation fuel: a comparison with hydrocarbon fuels. Int J Hydrogen Energy 1997;22:1053–60. https://doi.org/10.1016/S0360-3199(97)00008-6.
[2] Dunn S. Hydrogen futures: toward a sustainable energy system. Int J Hydrogen Energy 2002;27:235–64. https://doi.org/10.1016/S0360-3199(01)00131-8.
[3] Edwards PP, Kuznetsov VL, David WIF, Brandon NP. Hydrogen and fuel cells: towards a sustainable energy future. Energy Pol 2008;36:4356–62. https://doi.org/10.1016/j.enpol.2008.09.036.
[4] Yue M, Lambert H, Pahon E, Roche R, Jemei S, Hissel D. Hydrogen energy systems: a critical review of technologies, applications, trends and challenges. Renew Sustain Energy Rev 2021;146:111180. https://doi.org/10.1016/j.rser.2021.111180.
[5] Chi J, Yu H. Water electrolysis based on renewable energy for hydrogen production. Chin J Catal 2018;39:390–4. https://doi.org/10.1016/S1872-2067(17)62949-8.
[6] Pietro Reverberi A, Klemeš JJ, Varbanov PS, Fabiano B. A review on hydrogen production from hydrogen sulphide by chemical and photochemical methods. J Clean Prod 2016;136:72–80. https://doi.org/10.1016/j.jclepro.2016.04.139.
[7] Mishra P. Investigation and optimization of nanostructured TiO2 photoelectrode in regard to hydrogen production through photoelectrochemical process. Int J Hydrogen Energy 2003. https://doi.org/10.1016/S0360-3199(02)00197-0.
[8] Eroglu E, Melis A. Photobiological hydrogen production: recent advances and state of the art. Bioresour Technol 2011;102:8403–13. https://doi.org/10.1016/j.biortech.2011.03.026.
[9] Lindblom U. A conceptual design for compressed hydrogen storage in mined caverns. Int J Hydrogen Energy 1985;10:667–75. https://doi.org/10.1016/0360-3199(85)90006-0.
[10] Hosseini M, Dincer I, Naterer GF, Rosen MA. Thermodynamic analysis of filling compressed gaseous hydrogen storage tanks. Int J Hydrogen Energy 2012;37:5063–71. https://doi.org/10.1016/j.ijhydene.2011.12.047.
[11] Aceves S. Analytical and experimental evaluation of insulated pressure vessels for cryogenic hydrogen storage. Int J Hydrogen Energy 2000;25:1075–85. https://doi.org/10.1016/S0360-3199(00)00016-1.
[12] Hu Q, Lu Y, Meisner GP. Preparation of nanoporous carbon particles and their cryogenic hydrogen storage capacities. J Phys Chem C 2008;112:1516–23. https://doi.org/10.1021/jp076409t.
[13] Ahluwalia RK, Hua TQ, Peng J-K, Lasher S, McKenney K, Sinha J, et al. Technical assessment of cryo-compressed hydrogen storage tank systems for automotive applications. Int J Hydrogen Energy 2010;35:4171–84. https://doi.org/10.1016/j.ijhydene.2010.02.074.
[14] Allendorf MD, Hulvey Z, Gennett T, Ahmed A, Autrey T. Camp J, et al. An assessment of strategies for the development of solid-state adsorbents for vehicular hydrogen storage. Energy Environ Sci 2018;11:2784–812. https://doi.org/10.1039/C8EE01085D.
[15] Lee S-Y, Lee J-H, Kim Y-H, Kim J-W, Lee K-J, Park S-J. Recent progress using solid-state materials for hydrogen storage: a short review. Processes 2022;10:304. https://doi.org/10.3390/pr10020304.
[16] Xu W, Takahashi K, Matsuo Y, Hattori Y, Kumagai M, Ishiyama S, et al. Investigation of hydrogen storage capacity of various carbon materials. Int J Hydrogen Energy 2007;32:2504–12. https://doi.org/10.1016/j.ijhydene.2006.11.012.
[17] Zubizarreta L, Arenillas A, Pis JJ. Carbon materials for H2 storage. Int J Hydrogen Energy 2009;34:4575–81. https://doi.org/10.1016/j.ijhydene.2008.07.112.
[18] Dillon AC, Jones KM, Bekkedahl TA, Kiang CH, Bethune DS, Heben MJ. Storage of hydrogen in single-walled carbon nanotubes. Nature 1997;386:377–9. https://doi.org/10.1038/386377a0.
[19] Castaldo R, Avolio R, Cocca M, Gentile G, Errico ME, Avella M, et al. Synthesis and adsorption study of hyper-crosslinked styrene-based nanocomposites containing multi-walled carbon nanotubes. RSC Adv 2017;7:6865–74. https://doi.org/10.1039/C6RA25481K.
[20] Łodziana Z, Dębski A, Cios G, Budziak A. Ternary LaNi4.75M0.25 hydrogen storage alloys: surface segregation, hydrogen sorption and thermodynamic stability. Int J Hydrogen Energy 2019;44:1760–73. https://doi.org/10.1016/j.ijhydene.2018.11.104.
[21] Mbonu IJ, Louis H, Chukwu UG, Agwamba EC, Ghotekar S, Adeyinka AS. Effects of metals (X = Be, Mg, Ca) encapsulation on the structural, electronic, phonon, and hydrogen storage properties of KXCl3 halide perovskites: perspective from density functional theory. Int J Hydrogen Energy 2023. https://doi.org/10.1016/j.ijhydene.2023.07.099.
[22] Bhat VV, Rougier A, Aymard L, Darok X, Nazri G, Tarascon JM. Catalytic activity of oxides and halides on hydrogen storage of MgH2. J Power Sources 2006;159:107–10. https://doi.org/10.1016/j.jpowsour.2006.04.059.
[23] Anderson PA, Chater PA, Hewett DR, Slater PR. Hydrogen storage and ionic mobility in amide–halide systems. Faraday Discuss 2011;151:271. https://doi.org/10.1039/c0fd00027b.
[24] Yang Q, Zhong C. Molecular simulation of adsorption and diffusion of hydrogen in Metal−Organic frameworks. J Phys Chem B 2005;109:11862–4. https://doi.org/10.1021/jp051903n.
[25] Panella B, Hirscher M, Pütter H, Müller U. Hydrogen adsorption in metal–organic frameworks: Cu-MOFs and Zn-MOFs compared. Adv Funct Mater 2006;16:520–4. https://doi.org/10.1002/adfm.200500561.
[26] Kaye SS, Dailly A, Yaghi OM, Long JR. Impact of preparation and handling on the hydrogen storage properties of Zn 4 O(1,4-benzenedicarboxylate) 3 (MOF-5). J Am Chem Soc 2007;129:14176–7. https://doi.org/10.1021/ja076877g.
[27] Li Y, Yang RT. Hydrogen storage in low silica type X zeolites. J Phys Chem B 2006;110:17175–81. https://doi.org/10.1021/jp0634508.
[28] Stadie NP, Vajo JJ, Cumberland RW, Wilson AA, Ahn CC, Fultz B. Zeolite-templated carbon materials for high-pressure hydrogen storage. Langmuir 2012;28:10057–63. https://doi.org/10.1021/la302050m.
[29] Zhou J, Wang Q, Sun Q, Jena P, Chen XS. Electric field enhanced hydrogen storage on polarizable materials substrates. Proc Natl Acad Sci USA 2010;107:2801–6. https://doi.org/10.1073/pnas.0905571107.
[30] Guo X, Zhang X, Zhao S, Huang Q, Xue J. High adsorption capacity of heavy metals on two-dimensional MXenes: an ab initio study with molecular dynamics simulation. Phys Chem Chem Phys 2016;18:228–33. https://doi.org/10.1039/C5CP06078H.
[31] Liu X, Ma T, Pinna N, Zhang J. Two-dimensional nanostructured materials for gas sensing. Adv Funct Mater 2017;27:1702168. https://doi.org/10.1002/adfm.201702168.
[32] Li Y, Guo Y, Chen W, Jiao Z, Ma S. Reversible hydrogen storage behaviors of Ti2N MXenes predicted by first-principles calculations. J Mater Sci 2019;54:493–505. https://doi.org/10.1007/s10853-018-2854-7.
[33] Ao ZM, Peeters FM. High-capacity hydrogen storage in Al-adsorbed graphene. Phys Rev B 2010;81:205406. https://doi.org/10.1103/PhysRevB.81.205406.
[34] Fu P, Wang J, Jia R, Bibi S, Eglitis RI, Zhang H-X. Theoretical study on hydrogen storage capacity of expanded h-BN systems. Comput Mater Sci 2017;139:335–40. https://doi.org/10.1016/j.commatsci.2017.08.015.
[35] Haldar S, Mukherjee S, Singh CV. Hydrogen storage in Li, Na and Ca decorated and defective borophene: a first principles study. RSC Adv 2018;8:20748–57. https://doi.org/10.1039/C7RA12512G.
[36] Zhang H, Hu W, Du A, Lu X, Zhang Y, Zhou J, et al. Doped phosphorene for hydrogen capture: a DFT study. Appl Surf Sci 2018;433:249–55. https://doi.org/10.1016/j.apsusc.2017.09.243.
[37] Hussain T, Kaewmaraya T, Chakraborty S, Ahuja R. Functionalization of hydrogenated silicene with alkali and alkaline earth metals for efficient hydrogen storage. Phys Chem Chem Phys 2013;15:18900. https://doi.org/10.1039/c3cp52830h.
[38] Balaban AT. Heliphenes and related structures. Open Org Chem J 2011;5:117–26. https://doi.org/10.2174/1874364101105010117.
[39] Brunetto G, Autreto PAS, Machado LD, Santos BI, dos Santos RPB, Galvão DS. Nonzero gap two-dimensional carbon allotrope from porous graphene. J Phys Chem C 2012;116:12810–3. https://doi.org/10.1021/jp211300n.

[40] Yadav S, Tam J, Singh CV. A first principles study of hydrogen storage on lithium decorated two dimensional carbon allotropes. Int J Hydrogen Energy 2015;40:6128–36. https://doi.org/10.1016/j.ijhydene.2015.03.038.
[41] Boezar K, Reisi-Vanani A, Dehkhodaei M. Modification of graphenylene nanostructure with transition metals (Fe, Sc and Ti) to promote hydrogen storage ability: a DFT-D3 study. Int J Hydrogen Energy 2021;46:38370–80. https://doi.org/10.1016/j.ijhydene.2021.09.106.
[42] Fabris GSL, Marana NL, Longo E, Sambrano JR. Porous silicene and silicon graphenylene-like surfaces: a DFT study. Theor Chem Acc 2018;137:13. https://doi.org/10.1007/s00214-017-2188-6.
[43] Fabris GSL, Marana NL, Laranjeira JAS, Longo E, Sambrano JR. New two-dimensional zinc oxide nanosheets: properties, stability, and interconversion. Mater Lett 2020;275:128067. https://doi.org/10.1016/j.matlet.2020.128067.
[44] Fabris GSL, Marana NL, Longo E, Sambrano JR. Theoretical study of porous surfaces derived from graphene and boron nitride. J Solid State Chem 2018;258:247–55. https://doi.org/10.1016/j.jssc.2017.10.025.
[45] Martins NF, Laranjeira JAS, Azevedo SA, Fabris GSL, Sambrano JR. Structural, electronic and mechanical properties of a novel graphenylene-like structure based on GeC. J Phys Chem Solid 2023;181:111518. https://doi.org/10.1016/j.jpcs.2023.111518.
[46] Martins NF, Fabris GSL, Albuquerque AR, Sambrano JR. A new multifunctional two-dimensional monolayer based on silicon carbide. FlatChem 2021;30:100286. https://doi.org/10.1016/j.flatc.2021.100286.
[47] Martins NF, Fabris GSL, Maia AS, Albuquerque AR, Sambrano JR. Inorganic graphenylene-like silicon carbide as anode material for Na batteries. FlatChem 2022;35:100410. https://doi.org/10.1016/j.flatc.2022.100410.
[48] Dovesi R, Erba A, Orlando R, Zicovich-Wilson CM, Civalleri B, Maschio L, et al. Quantum-mechanical condensed matter simulations with CRYSTAL. WIREs Comput Mol Sci 2018;8. https://doi.org/10.1002/wcms.1360.
[49] Bilc DI, Orlando R, Shaltaf R, Rignanese GM, Íñiguez J, Ghosez P. Hybrid exchange-correlation functional for accurate prediction of the electronic and structural properties of ferroelectric oxides. Phys Rev B Condens Matter 2008;77:1–13. https://doi.org/10.1103/PhysRevB.77.165107.
[50] Peintinger MF, Oliveira DV, Bredow T. Consistent Gaussian basis sets of triple-zeta valence with polarization quality for solid-state calculations. J Comput Chem 2013;34:451–9. https://doi.org/10.1002/jcc.23153.
[51] Valenzano L, Torres FJ, Doll K, Pascale F, Zicovich-Wilson CM, Dovesi R. Ab initio study of the vibrational spectrum and related properties of crystalline compounds; the case of CaCO3 calcite. Zeitschrift Fur Phys Chemie 2006;220:893–912. https://doi.org/10.1524/zpch.2006.220.7.893.
[52] Martins NF, Fabris GSL, Albuquerque AR, Paupitz R, Sambrano JR. Graphenylene-like structures as a new class of multifunctional materials alternatives to graphene. 2022. p. 209–30. https://doi.org/10.1007/978-3-031-07622-0_7.
[53] Grimme S, Antony J, Ehrlich S, Krieg H. A consistent and accurate ab initio parametrization of density functional dispersion correction (DFT-D) for the 94 elements H-Pu. J Chem Phys 2010;132. https://doi.org/10.1063/1.3382344.
[54] Broyden CG. The convergence of a class of double-rank minimization algorithms 1. General considerations. IMA J Appl Math 1970;6:76–90. https://doi.org/10.1093/imamat/6.1.76.
[55] Monkhorst HJ, Pack JD. Special points for Brillouin-zone integrations. Phys Rev B 1976;13:5188–92. https://doi.org/10.1103/PhysRevB.13.5188.
[56] Gilat G, Raubenheimer LJ. Accurate numerical method for calculating frequency-distribution functions in solids. Phys Rev 1966;144:390–5. https://doi.org/10.1103/PhysRev.144.390.
[57] Bader RFW. Atoms in molecules. Acc Chem Res 1985;18:9–15. https://doi.org/10.1021/ar00109a003.
[58] Bader RFW, Essén H. The characterization of atomic interactions. J Chem Phys 1984;80:1943–60. https://doi.org/10.1063/1.446956.
[59] Gatti C. Chemical bonding in crystals: new directions. Z für Kristallogr - Cryst Mater 2005;220. https://doi.org/10.1524/zkri.220.5.399.65073.
[60] Silva JF, Fabris GSL, Sambrano JR, Albuquerque AR, Maia AS. scp>TopIso3D</scp> *viewer* : enhancing topological analysis through 3D isosurfaces. J Chem Inf Model 2023. https://doi.org/10.1021/acs.jcim.3c00302.
[61] Gatti C, Casassa S. TOPOND14 User's Manual. Milano: CNR-ISTM of Milano; 2013.
[62] van Duijneveldt FB, van Duijneveldt-van de Rijdt JGCM, van Lenthe JH. State of the art in counterpoise theory. Chem Rev 1994;94:1873–85. https://doi.org/10.1021/cr00031a007.
[63] Durbin DJ, Malardier-Jugroot C. Review of hydrogen storage techniques for on board vehicle applications. Int J Hydrogen Energy 2013;38:14595–617. https://doi.org/10.1016/j.ijhydene.2013.07.058.
[64] Alhameedi K, Karton A, Jayatilaka D, Hussain T. Metal functionalized inorganic nano-sheets as promising materials for clean energy storage. Appl Surf Sci 2019;471:887–92. https://doi.org/10.1016/j.apsusc.2018.12.036.
[65] Jat RA, Parida SC, Nuwad J, Agarwal R, Kulkarni SG. Hydrogen sorption–desorption studies on ZrCo–hydrogen system. J Therm Anal Calorim 2013;112:37–43. https://doi.org/10.1007/s10973-012-2783-7.
[66] EL Kassaoui M, Houmad M, Lakhal M, Benyoussef A, El Kenz A, Loulidi M. Hydrogen storage in lithium, sodium and magnesium-decorated on tetragonal silicon carbide. Int J Hydrogen Energy 2021;46:24190–201. https://doi.org/10.1016/j.ijhydene.2021.04.183.
[67] Gao H, Shi R, Shao Y, Liu Y, Zhu Y, Zhang J, et al. Catalysis derived from flower-like Ni MOF towards the hydrogen storage performance of magnesium hydride. Int J Hydrogen Energy 2022;47:9346–56. https://doi.org/10.1016/j.ijhydene.2022.01.020.
[68] Yadav MK, Panwar N, Singh S, Kumar P. Preheated self-aligned graphene oxide for enhanced room temperature hydrogen storage. Int J Hydrogen Energy 2020;45:19561–6. https://doi.org/10.1016/j.ijhydene.2020.05.083.
[69] Liu H, Yang S, Lei G, Xu M, Xu H, Lan Z, et al. Y-decorated MoS2 monolayer for promising hydrogen storage: a DFT study. Int J Hydrogen Energy 2022;47:12096–106. https://doi.org/10.1016/j.ijhydene.2022.01.236.
[70] Li X, Tan X, Xue Q, Smith S. Charge-controlled switchable H2 storage on conductive borophene nanosheet. Int J Hydrogen Energy 2019;44:20150–7. https://doi.org/10.1016/j.ijhydene.2019.05.225.
[71] Mohajeri A, Shahsavar A. Light metal decoration on nitrogen/sulfur codoped graphyne: an efficient strategy for designing hydrogen storage media. Phys E Low-Dimensional Syst Nanostructures 2018;101:167–73. https://doi.org/10.1016/j.physe.2018.04.007.
[72] Liu P-P, Zhang H, Cheng X-L, Tang Y-J. External electric field: an effective way to prevent aggregation of Mg atoms on γ-graphyne for high hydrogen storage capacity. Appl Surf Sci 2016;371:44–9. https://doi.org/10.1016/j.apsusc.2016.02.223.
[73] Hussain T, Hankel M, Searles DJ. Graphenylene monolayers doped with alkali or alkaline earth metals: promising materials for clean energy storage. J Phys Chem C 2017;121:14393–400. https://doi.org/10.1021/acs.jpcc.7b02191.
[74] Kaewmaraya T, Thatsami N, Tangpakonsab P, Kinkla R, Kotmool K, Menendez C, et al. Ultrahigh hydrogen storage using metal-decorated defected biphenylene. Appl Surf Sci 2023;629:157391. https://doi.org/10.1016/j.apsusc.2023.157391.
[75] Mane P, Kaur SP, Singh M, Kundu A, Chakraborty B. Superior hydrogen storage capacity of Vanadium decorated biphenylene (Bi+V): a DFT study. Int J Hydrogen Energy 2023;48:28076–90. https://doi.org/10.1016/j.ijhydene.2023.04.033.
[76] Pan R, Fan X, Luo Z, An Y. Calcium decorated two dimensional carbon allotropes for hydrogen storage: a first-principles study. Comput Mater Sci 2016;124:106–13. https://doi.org/10.1016/j.commatsci.2016.07.021.
[77] Chakraborty B, Ray P, Garg N, Banerjee S. High capacity reversible hydrogen storage in titanium doped 2D carbon allotrope Ψ-graphene: density Functional Theory investigations. Int J Hydrogen Energy 2021;46:4154–67. https://doi.org/10.1016/j.ijhydene.2020.10.161.
[78] Gao Y, Zhang H, Pan H, Li Q, Zhao J. Ultrahigh hydrogen storage capacity of holey graphyne. Nanotechnology 2021;32:215402. https://doi.org/10.1088/1361-6528/abe48d.
[79] Macchi P, Proserpio DM, Sironi A. Experimental electron density in a transition metal dimer: metal−Metal and Metal−Ligand bonds. J Am Chem Soc 1998;120:13429–35. https://doi.org/10.1021/ja982903m.
[80] Espinosa E, Alkorta I, Elguero J, Molins E. From weak to strong interactions: a comprehensive analysis of the topological and energetic properties of the electron density distribution involving X–H···F–Y systems. J Chem Phys 2002;117:5529–42. https://doi.org/10.1063/1.1501133.
[81] Yang L, Li X, Zhang G, Cui P, Wang X, Jiang X, et al. Combining photocatalytic hydrogen generation and capsule storage in graphene based sandwich structures. Nat Commun 2017;8:16049. https://doi.org/10.1038/ncomms16049.
[82] Kim TH, Bae J, Lee TH, Hwang J, Jung JH, Kim DK, et al. Room-temperature hydrogen storage via two-dimensional potential well in mesoporous graphene oxide. Nano Energy 2016;27:402–11. https://doi.org/10.1016/j.nanoen.2016.07.027.